AIMS Mathematics, 10(5): 12661–12688.
DOI: 10.3934/math.2025571
Received: 07 February 2025
Revised: 12 May 2025
Accepted: 20 May 2025
Published: 29 May 2025

https://www.aimspress.com/journal/Math

Research article

Transient thermoelastic responses in spherical elastic porous media using a fractional two-phase-lag model with space-time nonlocality

Kareem Alanazi and Ahmed E. Abouelregal*

Department of Mathematics, College of Science, Sakaka, Jouf University, 2014, Saudi Arabia; Email: k.alanazi@ju.edu.sa, ahabogal@ju.edu.sa

* **Correspondence:** Email: ahabogal@ju.edu.sa.

Abstract: This study investigated the impact of the fractional Caputo-tempered two-phase-lag (FCT-TPL) heat conduction model on thermoelastic vibrations within a medium containing spherical cavities and voids. In the proposed model, the nonlocality of time and space is integrated to unify classical and generalized thermoelastic theories, enabling a thorough investigation of size-dependent phenomena and the scattering characteristics of thermo-mechanical waves. Also, by integrating fractional calculus with tempered derivatives, the proposed model adeptly captures the complex interaction between localized thermal effects and nonlocal mechanical responses, particularly in materials with pronounced microstructural features. The fractional order and tempering parameter are shown to play a crucial role in controlling thermal relaxation times and the amplitude of thermoelastic vibrations. The findings reveal that the integration of the fractional Caputo-tempered derivative, along with temporal and spatial nonlocal effects, into the two-phase-lag model significantly improves the accuracy of predicting transient thermoelastic responses in materials with cavities and voids.

Keywords: space-time nonlocality; TPL model; voids; spherical cavities; Caputo-tempered fractional
Mathematics Subject Classification: 70J35, 35B44, 65M60, 74F10

1. Introduction

Thermoelasticity, which examines the interaction between thermal and mechanical properties in materials, has long been a cornerstone in the fields of materials science and engineering. Traditional thermoelastic theories, largely founded on Fourier's law of heat conduction, have laid the groundwork for the analysis of thermal stress and energy dissipation [1,2]. Nevertheless, these classical models

often fall short in accurately depicting the behavior of contemporary materials, particularly those with microstructural anomalies such as voids, cavities, or granular structures. These characteristics, frequently present in advanced composites, porous materials, and microelectromechanical systems (MEMS), create localized thermal gradients, contribute to wave scattering, and induce size-dependent phenomena, thereby challenging the validity of classical theoretical models [3].

To overcome these shortcomings, researchers have formulated generalized thermoelastic models, including the two-phase-lag (TPL) model [4–6], which accounts for time delays in the correlation between heat flux and temperature gradients. Moreover, Lord and Shulman [7] put forward a theory based on a revised heat conduction law that includes the rate of heat flux. At the same time, Green and Lindsay [8] established a theory that factors in the rate of temperature change as one of the constitutive variables. These generalized theories suggest that heat propagation should be understood as a wave-like phenomenon instead of solely a diffusion process, a concept frequently discussed in academic literature as the "second sound effect".

Although these cutting-edge models improve upon traditional methods, they frequently face challenges when addressing materials with nonlocal interactions, where both thermal and mechanical responses are shaped by spatial and temporal histories [9]. Furthermore, materials that display memory-dependent behavior require more sophisticated modeling approaches to accurately represent their intricate dynamics. These issues underscore the need for continued advancements in thermoelasticity to provide reliable predictions relevant to real-world applications. Nonlocal elasticity theories [10–14] have emerged as a notable breakthrough in materials science, particularly for analyzing the behavior of materials at the nanoscale. These theories introduce an internal length scale, which is essential for capturing size-dependent effects that classical elasticity models often fail to account for.

In recent years, the concept of spatiotemporal nonlocality has gained significant attention in physics and engineering, particularly in the study of nanoscale materials. Traditional local theories, which assume that a material's behavior at a given point is determined solely by its immediate surroundings, often fall short in accurately describing phenomena where size effects play a critical role [15]. Spatiotemporal nonlocality addresses these limitations by accounting for interactions that occur across both space and time, providing a more comprehensive framework to analyze complex material behaviors [16,17].

This approach is especially relevant for modeling phenomena such as wave propagation, thermal conduction, and mechanical deformation in nanostructured materials. By incorporating spatiotemporal nonlocality, researchers can better understand how microstructural features and boundary conditions significantly influence the overall behavior of materials at smaller scales [18]. This methodology captures the intricate interplay between distant regions and historical effects, which are often overlooked in classical models but are crucial for nanoscale systems [19,20].

The integration of spatiotemporal nonlocality into modeling frameworks allows for more accurate predictions of material responses under various loading conditions and environmental influences. This advancement not only enhances fundamental understanding but also opens new avenues for designing and optimizing advanced materials and structures [21]. As a result, it facilitates breakthroughs in diverse fields, including nanotechnology, aerospace engineering, and biomedical applications, among others, enabling the development of innovative technologies and solutions tailored to modern challenges.

Fractional derivatives generalize the concept of classical differentiation to non-integer orders, offering a robust mathematical framework for modeling processes that involve memory and hereditary effects. Among the various definitions of fractional derivatives, the Caputo derivative is one of the most commonly used, especially valued for its effectiveness in physical and engineering applications [22]. The emergence of non-singular fractional derivatives has attracted considerable interest in recent times, especially with the advent of Caputo–Fabrizio (CF) [23,24] and Atangana–Baleanu (AB) fractional

derivatives [25,26]. These groundbreaking methods provide versatile and powerful tools for accurately modeling intricate physical phenomena. The CF derivative, introduced by Caputo and Fabrizio, operates at a fractional order and is designed to address the limitations of traditional fractional derivatives that often involve singular kernels [23,24]. The AB fractional derivative [25,26] is based on the Mittag-Leffler kernel, which allows for non-singular behavior.

The introduction of tempered fractional derivatives (TF derivatives) marks an advancement in fractional calculus (FC), expanding traditional concepts to include exponential factors. This enhancement enables a more refined modeling of diverse physical phenomena, especially in systems where standard fractional derivatives may fall short in accurately capturing dynamic processes [27]. TF derivatives and integrals are formulated by incorporating an exponential factor into fractional derivatives and integrals. This adjustment brings about a tempering effect that modifies the behavior of these derivatives, making them applicable to a broader spectrum of scenarios [28]. A key application of TF derivatives lies in tempered fractional diffusion systems. In these settings, the conventional second-order derivative concerning spatial coordinates is substituted with a TF derivative, enabling the modeling of diffusion processes that showcase nonlocal and memory-dependent behaviors [29]. The parameters associated with irregular walk models featuring exponentially tempered power-law barrier distributions can be effectively characterized using TF derivatives, thereby improving the models' ability to capture intricate diffusion patterns. TF time derivatives, derived from the tempered power law for future instances, have demonstrated their usefulness across various scientific domains, including geophysics [30]. They support the modeling of phenomena such as wave propagation, heat transfer, and material behavior in atypical conditions.

In this paper, a novel model is introduced to address a critical gap in the existing literature on nonlocal thermal conduction in porous thermoelastic materials, offering both innovative improvements and substantial contributions to the field. Unlike previous approaches, the proposed framework integrates the dual-phase lag (TPL) theory with both spatial and temporal nonlocality, employing Caputo-tempered fractional derivatives to capture behavior that is simultaneously memory-dependent and reflective of microscopic scale effects. These advanced elements form a unified methodology for modeling thermomechanical phenomena in porous thermoelastic materials, overcoming challenges in accurately predicting energy dissipation, wave propagation, and thermomechanical coupling.

By effectively addressing the complexities of memory effects, the model provides predictions of material behavior that closely mirror real-world observations, thereby bridging theoretical concepts with practical applications. Furthermore, it strikes a critical balance between mathematical simplicity and physical accuracy, marking a significant advancement in the study and application of porous thermoelastic materials. This achievement not only deepens understanding but also enhances the design and optimization of engineering systems, facilitating a wide range of applications and paving the way for future research in this pivotal area.

The remainder of this paper is organized as follows: Section 2 presents the mathematical formulation of the fractional Caputo-tempered two-phase-lag (FCT-TPL) model. In Section 3, direct application of the proposed model is provided, along with the corresponding problem formulation. Section 4 describes the mathematical techniques utilized to solve the governing equations, while Section 5 introduces a numerical approach for computing the inverse transformations of the physical fields. Subsequently, Section 6 delivers numerical results, accompanied by insights and discussions regarding the impact of the fractional order, the smoothing parameter, and the specific geometric configurations. Finally, Section 7 concludes the paper by summarizing the key findings, exploring the practical implications of the results, and identifying potential directions for future research in this field.

2. Fractional nonlocal thermoelastic models for voided porous materials

Understanding the behavior of porous materials containing voids under thermal and mechanical loading is crucial and necessitates the use of fractional nonlocal thermoelastic models. These models provide a more accurate depiction of the complex responses exhibited by such materials, which cannot be captured by classical elasticity theories. By incorporating nonlocal effects and fractional derivatives, these models offer a comprehensive analysis of the interactions between thermal, mechanical, and void-related phenomena [31].

The governing equations for the linear homogeneous two-phase thermoelastic model with voids, which considers the displacement field u_i, the void volume fraction ϕ, and the temperature variation field θ in the absence of external forces, are expressed as follows [32]:

$$g = \xi_1\theta - \xi_2\phi - \nu e \tag{1}$$

where ξ_1 is a constitutive parameter related to thermal response, ξ_2 is the coupling parameter between voids and thermal effects, g denotes the void-related body force, $e = \varepsilon_{kk}$ refers to cubic dilation, and ν is the mechanical response parameter due to voids [33]:

$$h_i = p\phi_{,i}, \tag{2}$$

where p is a constitutive parameter related to the volume fraction and h_i are the components of the equilibrated stress tensor [34]:

$$\sigma_{ij} = \nu\phi\delta_{ij} - \beta\theta\delta_{ij} + \lambda\varepsilon_{kk}\delta_{ij} + 2\mu\varepsilon_{ij}, \tag{3}$$

where $\beta = (3\lambda + 2\mu)\alpha_t$ connects thermal and elastic properties, λ and μ are the Lamé parameters, α_t is the linear thermal expansion coefficient, and δ_{ij} is the Kronecker delta.

$$\varepsilon_{ij} = \frac{1}{2}\left(u_{i,j} + u_{j,i}\right), \tag{4}$$

where ε_{ij} are the strain tensor components.

Nonlocal elasticity, which considers the influence of surrounding material points on a material point's behavior, is particularly relevant for nanostructured materials where size effects are significant. The fundamental equations of nonlocal elasticity include spatial integrals that account for contributions from surrounding points, providing a more comprehensive understanding of material behavior at the nanoscale.

In this section, we establish the constitutive relations and field equations for nonlocal thermoelastic materials with voids based on fractional derivative heat transfer. The nonlocal force stress tensor $T_{kl}(\boldsymbol{P})$, equilibrated stress components $H_i(\boldsymbol{P})$, and equilibrated body force $G(\boldsymbol{P})$ are defined as [35,36]:

$$T_{kl}(\boldsymbol{P}) = \int \sigma_{kl}(\boldsymbol{P}')\hbar(|\boldsymbol{P} - \boldsymbol{P}'|)d\Omega(\boldsymbol{P}), \tag{5}$$

$$H_i(\boldsymbol{P}) = \int h_i(\boldsymbol{P}')\hbar(|\boldsymbol{P} - \boldsymbol{P}'|)d\Omega(\boldsymbol{P}'), \tag{6}$$

$$G(\boldsymbol{P}) = \int g(\boldsymbol{r}')\hbar(|\boldsymbol{P} - \boldsymbol{P}'|)d\Omega(\boldsymbol{P}'), \tag{7}$$

where $\hbar(|\boldsymbol{P} - \boldsymbol{P}'|)$ is the kernel function that incorporates nonlocal influences, and $|\boldsymbol{P} - \boldsymbol{P}'|$ is the

Euclidean distance between points $\boldsymbol{P}$ and $\boldsymbol{P}'$.

Inspired by Eringen's nonlocal elastic model and the Boltzmann superposition integral model, stress and strain are treated as convolution functions of time and space. This means the stress and strain at a reference point depend on historical data and the state of the material at all points within the domain. The mathematical representation of this concept is as follows [20,21]:

$$T_{kl}(\boldsymbol{P},t)=\int_{-\infty}^{t}\int_{\Omega}\hbar(|\boldsymbol{P}-\boldsymbol{P}'|,t-t')\sigma_{kl}(\boldsymbol{P}',t')d\Omega(\boldsymbol{P}')dt'. \tag{8}$$

The kernel function $\hbar(|\boldsymbol{P}-\boldsymbol{P}'|,t-t')$ determines the nature and extent of nonlocal interactions. It typically exhibits properties ensuring that the influence of distant points diminishes with increasing distance and time.

In the same vein, the nonlocal equilibrated stress components $H_i(\boldsymbol{P})$ and the equilibrated body force $G(\boldsymbol{P})$ can be derived as follows [37]:

$$H_i(\boldsymbol{P},t)=\int\hbar(|\boldsymbol{P}-\boldsymbol{P}'|,t-t')h_i(\boldsymbol{P}',t')d\Omega(\boldsymbol{P}')dt', \tag{9}$$

$$G(\boldsymbol{P},t)=\int\hbar(|\boldsymbol{r}-\boldsymbol{r}'|,t-t')g(\boldsymbol{P}',t')d\Omega(\boldsymbol{P}')dt'. \tag{10}$$

To further develop the nonlocal elasticity theory, we suggest employing the Klein-Gordon (KG) operator as a means to capture both spatial and temporal nonlocalities within the framework of nonlocal elasticity. The KG differential operator, denoted as Δ, is defined in the following manner [21,38]:

$$\Delta=1-\eta^2\nabla^2+\zeta^2\frac{\partial^2}{\partial t^2}. \tag{11}$$

Here, η represents the internal length scale parameter that is linked to spatial nonlocality, while ζ serves as the characteristic time scale that captures temporal nonlocality. Additionally, ∇^2 denotes the Laplacian operator, which addresses spatial variations within the model.

When the KG operator Δ is applied to the nonlocal stress tensor τ_{kl}, the equilibrated stress components H_i, and the equilibrated body force G, we arrive at the governing equations for isotropic materials within the framework of KG-type nonlocal elasticity [39,40]:

$$\left(1-\eta^2\nabla^2+\zeta^2\frac{\partial^2}{\partial t^2}\right)T_{kl}=\sigma_{kl}=(\nu\phi-\beta\theta+\lambda\varepsilon_{kk})\delta_{ij}+2\mu\varepsilon_{ij}, \tag{12}$$

$$\left(1-\eta^2\nabla^2+\zeta^2\frac{\partial^2}{\partial t^2}\right)G=g=-\xi_2\phi+\xi_1\theta-\nu e, \tag{13}$$

$$\left(1-\eta^2\nabla^2+\zeta^2\frac{\partial^2}{\partial t^2}\right)H_i=h_i=\alpha_1\phi_{,i}. \tag{14}$$

According to Newton's second law, the fundamental equation of motion can be expressed as:

$$\tau_{ij,j}+F_i=\rho\frac{\partial^2 u_i}{\partial t^2}. \tag{15}$$

By inserting Eq (12) into Eq (15), the equation of motion transforms into:

$$\mu u_{i,jj} + (\lambda + \mu) u_{j,ij} - \beta \theta_{,i} + \mathscr{v} \phi_{,i} = \rho \left(1 - \eta^2 \nabla^2 + \zeta^2 \frac{\partial^2}{\partial t^2} \right) \frac{\partial^2 u_i}{\partial t^2}. \tag{16}$$

In the absence of any external equilibrated body force, the volume fraction field equation is represented as [41]:

$$G = \rho \chi_1 \ddot{\phi} - H_{i,i}, \tag{17}$$

where χ_1 refers to the equilibrated inertia. By incorporating G from Eq (13) and H_i from Eq (14), the volume fraction field equation is modified to [42]:

$$p \phi_{,ii} - \xi_2 \phi + \xi_1 \theta - \mathscr{v} e = \chi_1 \rho \left(1 - \eta^2 \nabla^2 + \zeta^2 \frac{\partial^2}{\partial t^2} \right) \ddot{\varphi}. \tag{18}$$

The equation that represents the coupling between entropy (S), temperature (θ), and voids (ϕ) is expressed as [43]:

$$\rho T_0 S = \xi_1 T_0 \phi + \rho C_E \theta + \beta e, \tag{19}$$

where C_E represents specific heat at constant strain. The energy equation defines the regulation of heat balance by including factors like internal heat generation (S_0) and the components of heat flux (q_i) as follows [44]:

$$\rho T_0 \dot{S} = -q_{i,i} + S_0. \tag{20}$$

The TPL thermoelastic model builds upon Fourier's law by adding phase lags for heat flux (τ_q) and the temperature gradient (τ_θ), which can be expressed as [4–6]:

$$\left(1 + \tau_q \frac{\partial}{\partial t} \right) q_i = -K \left(1 + \tau_\theta \frac{\partial}{\partial t} \right) \theta_{,i}, \tag{21}$$

where K denotes the thermal conductivity.

To increase accuracy, fractional derivatives are incorporated into the TPL model, allowing for the representation of memory effects and interactions that are nonlocal in nature. The adjusted DPL equation that includes fractional derivatives is expressed as [45]:

$$\left(1 + \tau_q^\alpha D_t^\alpha \right) q_i = -K (1 + \tau_\theta^\alpha D_t^\alpha) \theta_{,i}. \tag{22}$$

In this context, D_t^α denotes a fractional derivative of order α that falls within the interval $(0,1)$, extending the notion of differentiation to include effects related to memory and heredity.

Various formulations of fractional derivatives are employed based on the specific requirements of each application. In this study, we will focus solely on two key examples of fractional operators. The Caputo fractional derivative of order α $(0 < \alpha < 1)$ for $Y(t)$ is defined as [46]:

$${}_0^C D_0^{(\alpha)} Y(t) = \frac{1}{\Gamma(1-\alpha)} \int_0^t \frac{1}{(t-\mathscr{s})^\alpha} \frac{d}{d\mathscr{s}} Y(\mathscr{s})\, d\mathscr{s}. \tag{23}$$

The Caputo-tempered fractional derivative of order α $(0 < \alpha < 1)$ with tempering parameter $\sigma > 0$ is defined as [47,48]:

$$ {}_0^{CT}D_t^{\alpha,\sigma}Y(t) = \frac{e^{-\sigma t}}{\Gamma(1-\alpha)}\int_0^t \frac{d}{d\mathcal{s}}\left(e^{\sigma \mathcal{s}}Y(\mathcal{s})\right)(t-\mathcal{s})^{-\alpha}\,d\mathcal{s}. \tag{24} $$

The Caputo-tempered fractional derivative incorporates a tempering parameter (σ) to adjust long-range memory effects. When σ is set to 0, it simplifies to the Caputo derivative. If σ is greater than 0, it adds an exponential tempering effect, which is perfect for systems that display declining memory characteristics. The CT derivative proves especially beneficial for materials that demonstrate both short-term and long-term memory behaviors.

Combining the fractional TPL model with the integrated thermal-mechanical framework allows us to derive the fractional heat conduction equation as follows:

$$ \left(1+\tau_q^{\alpha}D_t^{\alpha}\right)\left[\rho C_E\frac{\partial\theta}{\partial t}+\beta T_0\frac{\partial\varepsilon_{kk}}{\partial t}+\xi_1 T_0\frac{\partial\phi}{\partial t}-\frac{\partial Q}{\partial t}\right] = K(1+\tau_\theta^{\alpha}D_t^{\alpha})\theta_{,ii}. \tag{25} $$

3. Formulation of the problem

This study focuses on a nonlocal, homogeneous, isotropic thermoelastic medium described as infinite, containing a spherical cavity of radius R, where $R < r$ and r tends to infinity, filled with empty pores (see Figure 1). At the start, the surface of the cavity is held at a constant temperature T_0, with neither stress nor deformation present. The cavity's center is designated as the origin in the spherical polar coordinate system (r, Θ, Φ). In this coordinate setup, the body exhibits symmetrical characteristics, and the displacement components are simply defined as $u_r = u(r,t)$, while both u_Θ and u_Φ are zero. This expression arises due to the spherical symmetry of the problem. This configuration is based on the assumption that there are no body forces, external heat sources, or outside equilibrium forces acting on the system.

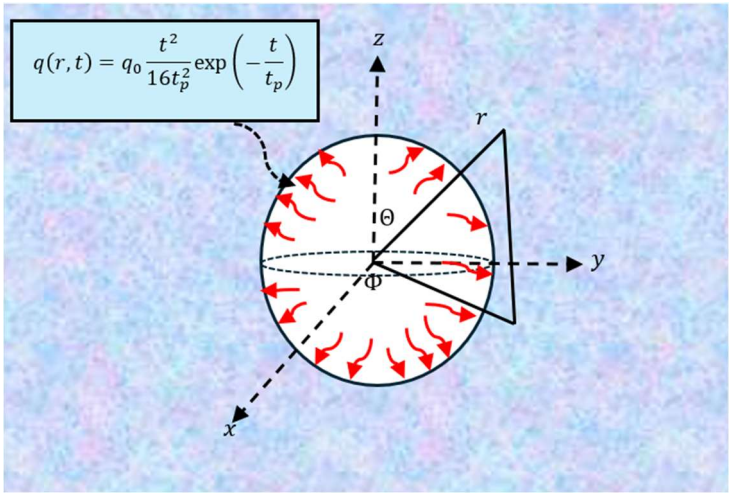

Figure 1. Schematic of a thermoelastic infinite medium with a spherical cavity and embedded voids.

The components of the strain tensor can be expressed as follows:

$$\varepsilon_{rr} = \frac{\partial u}{\partial r}, \varepsilon_{\Theta\Theta} = \varepsilon_{\Phi\Phi} = \frac{u}{r}, \varepsilon_{r\Phi} = \varepsilon_{r\Theta} = \varepsilon_{\Theta\Phi} = 0. \tag{26}$$

Based on this arrangement, the cubic dilatation e is characterized as:

$$e = \varepsilon_{kk} = \frac{\partial u}{\partial r} + \frac{2u}{r} = \frac{1}{r^2}\frac{\partial (r^2 u)}{\partial r}. \tag{27}$$

The nonlocal constitutive relationships (12) in the spherical polar coordinate system can be expressed as:

$$\begin{aligned} \left(1 - \eta^2\nabla^2 + \zeta^2\frac{\partial^2}{\partial t^2}\right) T_{rr} = \sigma_{rr} = 2\mu\frac{\partial u}{\partial r} + \lambda e + \nu\phi - \beta\theta, \\ \left(1 - \eta^2\nabla^2 + \zeta^2\frac{\partial^2}{\partial t^2}\right) T_{\Theta\Theta} = \sigma_{\Phi\Phi} = 2\mu\frac{u}{r} + \lambda e + \nu\phi - \beta\theta. \end{aligned} \tag{28}$$

Here, in spherical coordinates, the operator ∇^2 is defined as:

$$\nabla^2 = \frac{\partial^2}{\partial r^2} + \frac{2}{r}\frac{\partial}{\partial r}. \tag{29}$$

Consequently, the motion equation in spherical coordinates can be defined as:

$$T_{rr,r} + \frac{2}{r}\left(T_{rr} - T_{\psi\psi}\right) = \rho\frac{\partial^2 u}{\partial t^2}. \tag{30}$$

Moreover, the volume fraction field equation (18) linked to the voids can be rephrased as:

$$p\nabla^2\phi - \nu e - \xi_2\phi + \xi_1\theta = \rho\chi_1\left(1 - \eta^2\nabla^2 + \zeta^2\frac{\partial^2}{\partial t^2}\right)\frac{\partial^2\phi}{\partial t^2}. \tag{31}$$

By substituting Eq (28) into Eq (30), we derive:

$$(\lambda + 2\mu)\left(\frac{\partial^2 u}{\partial r^2} + \frac{1}{r}\frac{\partial u}{\partial r} - \frac{2u}{r^2}\right) + \left(\nu\frac{\partial\phi}{\partial r} - \beta\frac{\partial\theta}{\partial r}\right) = \rho\left(1 - \eta^2\nabla^2 + \zeta^2\frac{\partial^2}{\partial t^2}\right)\frac{\partial^2 u}{\partial t^2}. \tag{32}$$

Taking the divergence of Eq (32) results in:

$$(\lambda + 2\mu)\nabla^2 e + (\nu\nabla^2\phi - \beta\nabla^2\theta) = \rho\left(1 - \eta^2\nabla^2 + \zeta^2\frac{\partial^2}{\partial t^2}\right)\frac{\partial^2 e}{\partial t^2}. \tag{33}$$

The revised fractional TPL heat transfer equation can be articulated as:

$$K(1 + \tau_\theta^\alpha D_t^\alpha)\nabla^2\theta = \left(1 + \tau_q^\alpha D_t^\alpha\right)\left[\rho C_E\frac{\partial\theta}{\partial t} + \xi_1 T_0\frac{\partial\phi}{\partial t} + \beta T_0\frac{\partial e}{\partial t}\right]. \tag{34}$$

4. Initial and boundary conditions

Assuming the medium starts from rest, the following initial conditions are set:

$$\begin{aligned} \phi(r,0) = 0, \frac{\partial\phi(r,0)}{\partial t} = 0, \theta(x,0) = 0, \frac{\partial\theta(r,0)}{\partial t} = 0, \\ \tau_{ij}(r,0) = 0, \frac{\partial\tau_{ij}(r,0)}{\partial t} = 0, u(r,0) = 0, \frac{\partial u(r,0)}{\partial t} = 0. \end{aligned} \tag{35}$$

It is assumed that the surface of the medium is free of traction, with no voids crossing the boundary. Thus, the following mechanical boundary conditions are established:

$$T_{rr}(x,t) = 0, \ \frac{\partial\phi(r,t)}{\partial r} = 0 \quad \text{at} \quad r = R. \tag{36}$$

The surface of the cavity at $r = \mathrm{R}$ is expected to experience a pulsed heat flux. Therefore, the thermal boundary condition can be formulated as [49]:

$$-K\frac{\partial\theta(r,t)}{\partial r} = q_0\frac{t^2}{16t_p^2}\exp\left(-\frac{t}{t_p}\right) \quad \text{at} \quad r = R, \tag{37}$$

where q_0 indicates the peak intensity of the applied heat flux, and t_p serves as a time parameter designed to regulate the rise and fall rates of the pulse.

Utilizing the modified Fourier's law (23), the thermal condition can be represented as:

$$-K(1+\tau_\theta^\alpha D_t^\alpha)\frac{\partial\theta(r,t)}{\partial r} = q_0\left(1+\tau_q^\alpha D_t^\alpha\right)\left[\frac{t^2}{16t_p^2}\mathrm{e}^{\left(-\frac{t}{t_p}\right)}\right] \quad \text{at} \quad r = R. \tag{38}$$

5. Non-dimensional variables

To create a non-dimensional formulation for the thermoelastic porous half-space, we introduce non-dimensional variables that simplify the equations and highlight the crucial parameters influencing the system's behavior, particularly how voids affect thermal and mechanical interactions. The following non-dimensional variables will be defined based on the characteristic scales of the problem:

$$\begin{gathered}(r',u',\ell') = \upsilon_1\,\eta_1(r,u,\ell),\ \left(t',\tau_q',\tau_\theta',\tau'\right) = \upsilon_1^2\,\eta_1\left(t,\tau_q,\tau_\theta,\tau\right),\ \varphi' = \chi_1\upsilon_1^2\eta_1^2\varphi,\\ \tau_{ij}' = \frac{\tau_{ij}}{\upsilon_1^2\rho},\ \theta' = \frac{\beta\theta}{\upsilon_1^2\rho},\ \eta_1 = \frac{\rho C_E}{K}, p' = \frac{p}{\upsilon_1^2\chi_1\rho},\ \upsilon_1^2 = \frac{\lambda+2\mu}{\rho}.\end{gathered} \tag{39}$$

The governing Eqs (29), (31), (33), and (34) can thus be expressed in non-dimensional form as follows:

$$\begin{gathered}\left(1-\eta^2\nabla^2+\zeta^2\frac{\partial^2}{\partial t^2}\right)T_{rr} = \Upsilon_1\,\frac{\partial u}{\partial r}+\Upsilon_2 e+\mathcal{R}_1\phi-\theta,\\ \left(1-\eta^2\nabla^2+\zeta^2\frac{\partial^2}{\partial t^2}\right)T_{\Theta\Theta}\ =\ \Upsilon_1\frac{u}{r}+\Upsilon_2 e+\mathcal{R}_1\phi-\theta,\end{gathered} \tag{40}$$

$$\nabla^2 e+\mathcal{R}_1\nabla^2\phi-\nabla^2\theta\ = \left(1-\eta^2\nabla^2+\zeta^2\frac{\partial^2}{\partial t^2}\right)\frac{\partial^2 e}{\partial t^2}, \tag{41}$$

$$p\nabla^2\phi-\mathcal{R}_5 e-\mathcal{R}_4\phi\ +\mathcal{R}_6\theta = \left(1-\eta^2\nabla^2+\zeta^2\frac{\partial^2}{\partial t^2}\right)\frac{\partial^2\phi}{\partial t^2}, \tag{42}$$

$$(1+\tau_\theta^\alpha D_t^\alpha)\nabla^2\theta = \left(1+\tau_q^\alpha D_t^\alpha\right)\left[\mathcal{R}_2\frac{\partial e}{\partial t}+\mathcal{R}_3\frac{\partial\phi}{\partial t}+\frac{\partial\theta}{\partial t}\right], \tag{43}$$

where

$$\begin{gathered}\mathcal{R}_1 = \frac{\nu}{\upsilon_1^4\eta_1^2\chi_1\rho}, \mathcal{R}_2 = \frac{T_0\beta^2}{\upsilon_1^2\eta_1}, \mathcal{R}_3 = \frac{\xi_1 T_0\beta}{\upsilon_1^4\eta_1^3\chi_1\rho K}, \mathcal{R}_4 = \frac{\xi_2}{\upsilon_1^4\eta_1^2\chi_1\rho},\\ \mathcal{R}_5 = \frac{\nu}{\upsilon_1^2\rho}, \mathcal{R}_6 = \frac{m}{\beta}, \Upsilon_1 = \frac{2\mu}{\lambda+2\mu}, \Upsilon_2 = \frac{\lambda}{\lambda+2\mu}.\end{gathered} \tag{44}$$

6. Approach to solving the system of governing equations

The solution method involves converting the system of coupled partial differential equations (PDEs) into ordinary differential equations (ODEs) by utilizing the Laplace transform. The Laplace transform for a function $g(x,t)$, which varies with time t, is defined as:

$$\bar{g}(x,s) = \mathcal{L}[g(x,t)] = \int_0^\infty e^{-st}\,g(x,t)dt. \tag{45}$$

Applying the Laplace transform to the governing Eqs (40) through (43), while incorporating the initial conditions specified in Eq (35), leads to the derivation of the following transformed equations:

$$\begin{aligned}(1-\lambda_0\nabla^2)\bar{T}_{rr} &= \mathcal{Q}_1\frac{d\bar{u}}{dr}+\mathcal{Q}_0\frac{\bar{u}}{r}+\mathcal{Q}_3\bar{\phi}-\mathcal{Q}_2\bar{\theta},\\ (1-\lambda_0\nabla^2)\bar{T}_{\Theta\Theta} &= \mathcal{Q}_0\frac{d\bar{u}}{dr}+\mathcal{Q}_1\frac{\bar{u}}{r}+\mathcal{Q}_3\bar{\phi}-\mathcal{Q}_2\bar{\theta},\end{aligned} \tag{46}$$

$$(\nabla^2-\mathcal{Q}_4)\bar{e}=\mathcal{Q}_5\nabla^2\bar{\theta}-\mathcal{Q}_6\nabla^2\phi, \tag{47}$$

$$\left(\frac{d^2}{dx^2}-\mathcal{Q}_0\right)\bar{\theta}=\mathcal{Q}_7\bar{e}+\varpi_0\mathcal{R}_3\bar{\phi}, \tag{48}$$

$$(\nabla^2-\mathcal{Q}_9)\bar{\phi}=\mathcal{Q}_8\bar{e}-\mathcal{Q}_{10}\bar{\theta}, \tag{49}$$

where

$$\begin{gathered}\mathcal{Q}_0=\frac{\Upsilon_2}{1+\zeta^2s^2},\mathcal{Q}_1=\frac{\Upsilon_1}{1+\zeta^2s^2},\mathcal{Q}_2=\frac{1}{1+\zeta^2s^2},\mathcal{Q}_3=\frac{\mathcal{R}_1}{1+\zeta^2s^2},\mathcal{Q}_4=\frac{s^2(1+\zeta^2s^2)}{1+\eta^2s^2},\\ \mathcal{Q}_5=\frac{1}{1+\eta^2s^2},\mathcal{Q}_6=\frac{\mathcal{R}_1}{1+\eta^2s^2},\mathcal{Q}_7=\varpi_0\delta_2,\varpi_0=\frac{s\left(1+\tau_q\mathcal{F}(s)\right)}{\left(1+\tau_\theta\mathcal{F}(s)\right)},\\ \mathcal{Q}_8=\frac{\mathcal{R}_5}{p+\eta^2s^2},\mathcal{Q}_9=\frac{s^2(1+\zeta^2s^2)+\mathcal{R}_4}{p+\eta^2s^2},\mathcal{Q}_{10}=\frac{\mathcal{R}_6}{p+\eta^2s^2},\lambda_0=\frac{\eta^2}{1+\zeta^2s^2}.\end{gathered} \tag{50}$$

The transformed fractional operator $\mathcal{F}(s)$ is defined based on the type of fractional derivative used:

$$\mathcal{M}(s)=\begin{cases}\mathrm{s}^\alpha & \text{for C fractional operotor,}\\ (\mathrm{s}+\sigma)^\alpha & \text{for CT fractional operotor.}\end{cases} \tag{51}$$

By combining Eqs (47) to (49), we obtain the following sixth-order DE:

$$(\nabla^6-L_1\nabla^4+L_2\nabla^2-L_3)\bar{\mathcal{G}}=0, \tag{52}$$

where $\bar{\mathcal{G}}=\{\bar{e},\bar{\theta},\bar{\phi}\}$ and coefficients L_1, L_2, and L_3 are defined as:

$$\begin{aligned}L_1&=\frac{1}{\mathcal{Q}_7}[p_5+\mathcal{Q}_7p_1+\mathcal{Q}_8p_2],\\ L_2&=\frac{1}{\mathcal{Q}_7}[p_1p_5+\mathcal{Q}_7\mathcal{Q}_4\mathcal{Q}_0+p_2p_4+\mathcal{Q}_8p_3],\\ L_3&=\frac{1}{\mathcal{Q}_7}[\mathcal{Q}_4\mathcal{Q}_0p_5+p_3p_4].\end{aligned} \tag{53}$$

Here,

$$\begin{gathered}p_1=\mathcal{Q}_4+\varpi_0+\mathcal{Q}_5\mathcal{Q}_7,p_2=\varpi_0\mathcal{R}_3-\mathcal{Q}_6\mathcal{Q}_7,p_3=\mathcal{Q}_4\varpi_0\delta_3,\\ p_4=\mathcal{Q}_8\varpi_0+\mathcal{Q}_7\mathcal{Q}_{10},p_5=\mathcal{Q}_9\mathcal{Q}_7-\mathcal{Q}_8\varpi_0\mathcal{R}_3.\end{gathered} \tag{54}$$

The DE (52) can be expressed as the product of three second-order factors:

$$(\nabla^2-m_1^2)(\nabla^2-m_2^2)(\nabla^2-m_3^2)\{\bar{e},\bar{\theta},\bar{\phi}\}=0, \tag{55}$$

where m_1^2, m_2^2, and m_3^2 are roots with positive real parts of the characteristic equation:

$$m^6-L_1m^4+L_2m^2-L_3=0. \tag{56}$$

The formulation of the solution to Eq (55), under the condition that the variables remain finite as r approaches infinity, can be expressed as follows:

$$\{\bar{\theta},\bar{\phi},\bar{e}\}=\frac{1}{\sqrt{r}}\sum_{i=1}^{3}\{1,\Psi_i,\Gamma_i\}C_i\,K_{1/2}(m_ir). \tag{57}$$

Here, C_i represent constants that are established based on the boundary conditions, while Ψ_i and Γ_i are outlined as follows:

$$\Psi_i = \frac{m_i^4 - p_1 m_i^2 + Q_4 \mathcal{M}_0}{p_2 m_i^2 - p_3}, \Gamma_i = \frac{m_i^2 (Q_5 - Q_4 \Psi_i)}{m_i^2 - Q_4}, \quad i = 1,2,3. \tag{58}$$

By transforming Eq (27) using the Laplace transform and leveraging Eq (59), we can perform an integration with respect to r to derive the displacement $\bar{u}$ as follows:

$$\bar{u} = -\frac{1}{\sqrt{r}} \sum_{i=1}^{3} \frac{\Gamma_i}{m_i} C_i K_{3/2}(m_i r). \tag{59}$$

In the process of deriving Eq (59), the following relation for the modified Bessel functions of the second kind has been utilized:

$$\frac{d}{dr} K_{1/2}(m_i r) = \frac{1}{2r} K_{1/2}(m_i r) - m_i K_{3/2}(m_i r). \tag{60}$$

As $\mathcal{Y}$ becomes large, the modified Bessel functions of the second kind behave asymptotically as follows:

$$K_{1/2}(\mathcal{Y}) \sim \mathrm{e}^{-\mathcal{Y}} \sqrt{\frac{\pi}{2\mathcal{Y}}}, \quad K_{\frac{3}{2}}(\mathcal{Y}) = \mathrm{e}^{-\mathcal{Y}} \sqrt{\frac{\pi}{2\mathcal{Y}}} \left(1 + \frac{1}{\mathcal{Y}}\right). \tag{61}$$

When the asymptotic relations (50) are substituted into Eqs (46) and (49), we derive:

$$\{\bar{\theta}, \bar{\phi}, \bar{e}\} = \frac{1}{\sqrt{r}} \sum_{i=1}^{3} \{1, \Psi_i, \Gamma_i\} C_i \mathrm{e}^{-m_i r} \sqrt{\frac{\pi}{2m_i r}}, \tag{62}$$

$$\bar{u} = -\frac{1}{\sqrt{r}} \sum_{i=1}^{2} \frac{\Gamma_i}{m_i} C_i \mathrm{e}^{-m_i r} \sqrt{\frac{\pi}{2m_i r}} \left(1 + \frac{1}{2m_i r}\right). \tag{63}$$

Ultimately, by inserting Eqs (62) and (63) into Eq (46), we are able to determine the distributions of thermal stress.

Once the Laplace transform has been applied to the boundary conditions specified in Eqs (36) and (38), they are reformulated accordingly:

$$\bar{\tau}_{rr}(r, s) = 0, \ \frac{d\bar{\phi}(r,s)}{dr} = 0 \quad \text{at} \quad r = \mathrm{R}, \tag{64}$$

$$\frac{d\bar{\theta}(r,t)}{dr} = -\frac{\delta_0 q_0 t_p}{8(s t_p + 1)^3} = -\bar{G}(s) \quad \text{at} \quad r = \mathrm{R}. \tag{65}$$

To ascertain the values of constants C_1, C_2, and C_3, we substitute the functions $\bar{\tau}_{rr}$, $\bar{\phi}$, and $\bar{\theta}$ into the boundary conditions and solve the resulting system of equations. With this approach, we have successfully obtained the solutions across the entire domain within the Laplace transform space.

7. Converting solutions from Laplace domain to time domain

The Gaver-Stehfest method serves as an efficient numerical technique widely utilized in engineering and applied sciences for inverting the Laplace transform. This approach facilitates the transition from the Laplace domain into the physical domain, addressing both spatial and temporal variables. By combining numerical techniques with the essential features of the Laplace transform, this method provides a reliable way to compute inverse transforms, particularly for functions that are difficult to invert analytically.

The Gaver-Stehfest method can be employed to estimate the values of $g(r,t)$ at different time intervals through the following formula [50]:

$$g(r,t) \approx \frac{\ln(2)}{t}\sum_{k=1}^{N}\omega_k \bar{g}\left(r,\frac{n}{t}\ln(2)\right), k \geq 1,\ t > 0. \tag{66}$$

In this scenario, ω_k signifies the coefficients linked to the individual terms within the series expansion, and N denotes the total count of terms that are incorporated into the expansion; a number that is required to be even. The determination of the coefficients ω_k is based exclusively on the quantity of expansion terms k, and they are defined in the manner described as [51]:

$$\omega_k = (-1)^{k+\frac{N}{2}}\sum_{j=\frac{k+1}{2}}^{min\{k,N/2\}}\frac{j^{\frac{N}{2}}(2j)!}{\left(\frac{N}{2}-j\right)!(k-j)!(2j-k)!(j-1)!j!}, \quad k \geq 1, \quad 1 \leq N \leq k. \tag{67}$$

The Gaver-Stehfest method is particularly advantageous for its use in numerical analysis due to several key benefits. Its primary advantage is its efficiency. The method uses a straightforward summation formula, bypassing the more intricate processes of contour integration or symbolic inversion, thereby substantially decreasing the time required for computations. Furthermore, it is highly adaptable, being able to handle a wide array of Laplace-transformed functions that are commonly found in areas such as heat conduction, diffusion, and fluid dynamics. When it comes to smooth functions in the Laplace domain that are free from singularities or discontinuities, the Gaver-Stehfest method is capable of providing highly precise outcomes [52]. The simplicity of its formula also makes it accessible and easy to incorporate into numerical algorithms.

Nevertheless, the method is not without its drawbacks. A primary issue is numerical instability. As the parameter N is raised, the factorial elements within the coefficients ω_k can increase sharply, leading to a decrease in precision. Additionally, if the Laplace-domain function $\bar{g}(r,s)$ possesses singularities or discontinuities, the method's accuracy may be compromised. It is crucial to carefully select the value of N. While a higher N can improve precision for smooth functions, extremely large values of N might exacerbate numerical instability, potentially leading to difficulties in achieving dependable results.

8. Numerical results and analysis

This section focuses on the numerical simulation of the thermoelastic behavior of an infinite porous magnesium elastic body with a spherical cavity. The main goal is to validate the nonlocal thermoelastic model, which integrates spatial and temporal effects, fractional derivatives, and phase delays. Through this analysis, we aim to enhance our understanding of the interactions among different field variables and examine how the key model parameters affect the dynamic and transient responses of the material within the medium. For the simulations, we have utilized the unique material properties of porous elastic magnesium, a material commonly employed in mechanical and thermal engineering applications. The details of the material parameters are presented in Table 1:

Table 1. Material constants required for numerical simulations (magnesium) [53,54].

Property	Symbol	Value	Units
First Lamé parameter	λ	2.17×10^{10}	$\mathrm{Nm^{-2}}$
Shear modulus	μ	3.278×10^{10}	$\mathrm{Nm^{-2}}$
Density	ρ	1740	$\mathrm{kg/m^3}$
Void-strain coupling parameter	$\mathcal{V}$	1.13849×10^{10}	$\mathrm{Nm^{-2}}$
Void coupling parameter	ξ_2	1.475×10^{10}	$\mathrm{Nm^{-2}}$
Thermal conductivity	K	1.7×10^{2}	$\mathrm{Wm^{-2}K^{-1}}$
Thermal coupling coefficient	β	2.68×10^{6}	$\mathrm{Nm^{-2}K^{-1}}$
Thermal expansion coefficient	α_t	2.5×10^{-5}	$\mathrm{K^{-1}}$
Specific heat capacity	C_e	1.04×10^{10}	$\mathrm{J\ kg\ K^{-1}}$
Reference temperature	T_0	298	K
Void-thermal coupling parameter	ξ_1	2×10^{6}	$\mathrm{Nm^{-2}K^{-1}}$
Void density parameter	χ_1	1.753×10^{-15}	$\mathrm{m^2}$
Void interaction parameter	p	3.688×10^{-5}	N
Wave speed parameter	v_1^2	5.92×10^{6}	$\mathrm{m^2s^{-2}}$
Thermal diffusivity	η_1	1.065×10^{11}	$\mathrm{s^{-1}}$

In this study, the parameters governing the system's behavior are crucial for understanding the material's response to thermal and mechanical stimuli. The fractional order (α) is a pivotal factor that determines the extent of memory effects in the material. Lower α values enhance long-term memory, while higher values diminish these effects. The tempering parameter (σ) introduces exponential decay to the material's response, with higher values limiting long-range interactions and wave scattering, and lower values amplifying nonlocal interactions and wave dispersion.

Nonlocal parameters, such as spatial nonlocality (η) and temporal nonlocality (ζ), are essential for capturing size-dependent mechanical behavior and transient thermal effects. The spatial nonlocal parameter (η) dictates the localization of the material's response—smaller η values yield more localized effects, whereas larger values produce smoother, broader responses. The temporal nonlocal parameter (ζ) governs the material's reaction speed, influencing wave propagation rates.

Lastly, phase lags (τ_q and τ_θ) are critical for describing time delays in the material's thermal and heat flux responses. These lags contribute to the relaxation behavior, reducing vibration amplitudes; larger phase lags lead to longer relaxation times. Together, these parameters are integral to the model's precision and its capacity to predict the material's behavior under varying conditions.

8.1. Comparison of fractional derivatives in thermoelastic response

In this section, we analyze the numerical results to compare the behaviors of physical fields under two types of fractional derivatives: the fractional-Caputo derivative (C) and the tempered-Caputo fractional derivative (CT). By varying the fractional order (α) and the exponential tempering parameter (σ), we aim to clarify the impact of memory effects on the thermoelastic responses of porous materials. The results, presented in Figures 2 to 5, focus on critical physical quantities such as temperature (θ), radial displacement (u), nonlocal thermal stresses (T_{rr} and $T_{\Theta\Theta}$), and the volume fraction field (ϕ), as influenced by the chosen fractional operators.

Figure 2 specifically illustrates the variation of the temperature field (θ) based on the type of fractional derivative, the fractional order (α), and the tempering parameter (σ). One notable

observation is the effect of the fractional order: when employing the Caputo fractional derivative (C-TPL), reducing α from 1.0 to 0.5 causes a significant decrease in temperature values across all radial distances (r). This trend indicates that lower fractional orders enhance memory effects, resulting in more gradual thermal diffusion and lower peak temperatures. Additionally, the tempering parameter (σ) plays a critical role. With the tempered-Caputo fractional derivative (CT-TPL), increasing σ correlates with a further reduction in temperature values. For instance, at $\alpha = 0.5$, as σ increases from 0 to 20, the temperature drops considerably, suggesting that the effect of exponential tempering accelerates thermal memory decay, leading to faster attenuation of temperature profiles.

Moreover, when comparing the C-TPL and CT-TPL models, it becomes evident that the tempered-Caputo fractional derivative consistently results in lower temperature values than the traditional Caputo fractional derivative for the same fractional order (α). This observation highlights the additional damping effect introduced by the tempering parameter (σ), especially pronounced at larger radial distances (r). Lastly, the dependence of temperature (θ) on radial distance (r) is notable, showing a consistent decrease as r increases for all scenarios. However, the decay rate is affected by both the fractional order (α) and tempering parameter (σ). Lower values of α and higher values of σ lead to steeper declines in temperature, reflecting stronger memory effects and quicker thermal relaxation. These observations underscore the critical role of fractional calculus and tempering parameters in modeling thermoelastic responses. The ability to tune memory effects and thermal relaxation through α and σ provides a powerful tool for designing advanced materials with optimized thermoelastic properties. This study highlights how fractional operators, especially the tempered-Caputo derivative, enhance the accuracy and flexibility of modeling thermoelastic behaviors in porous materials.

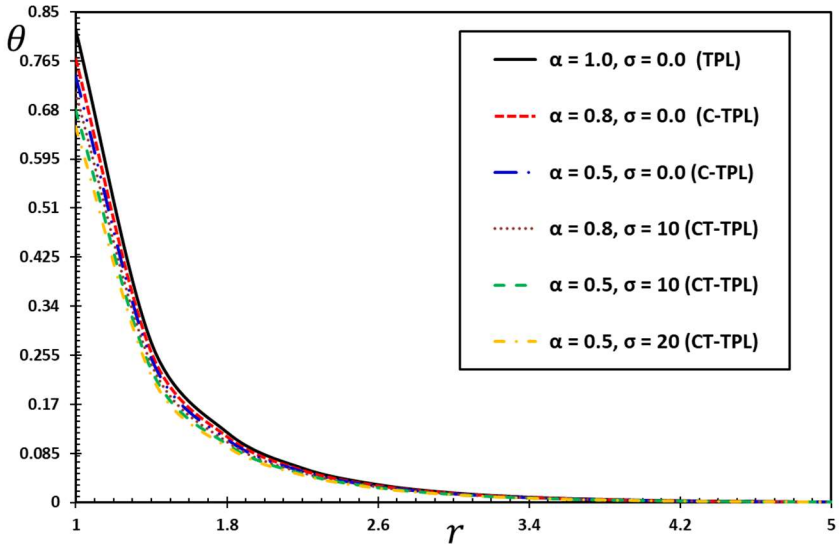

Figure 2. Temperature (θ) variations with fractional order (α) and tempering (σ) parameters.

Figure 3 illustrates the radial displacement (u) and how it is influenced by the type of fractional derivative, as well as the fractional order (α) and the exponential tempering parameter (σ). The examination of these parameters reveals significant trends in how displacement behaves within the porous medium. As the fractional order (α) is adjusted, variations in displacement patterns become evident, suggesting that the nature of memory effects plays a pivotal role in how the material responds. When the tempering parameter (σ) is held constant at 0.0, a reduction in the fractional order (α) from

1.0 to 0.5 leads to a marked decrease in the magnitude of radial displacement (u) across all radial distances (r). For instance, at $r = 1$, u changes from -0.590416 (for $\alpha = 1.0$) to -0.511017 (for $\alpha = 0.5$). This trend suggests that lower fractional orders ($\alpha < 1$) enhance memory effects, resulting in slower changes in displacement and a greater retention of previous mechanical states. In contrast, as α approaches 1, the displacement stabilizes more rapidly, reflecting a behavior similar to classical elasticity with diminished memory influences.

With a fixed fractional order (α), increasing the tempering parameter (σ) leads to a reduction in the magnitude of radial displacement (u). For example, at $r = 1$ and $\alpha = 0.5$, u decreases from -0.511017 (for $\sigma = 0.0$) to -0.383079 (for $\sigma = 20$). The exponential tempering factor $e^{-\sigma}$ speeds up the decay of memory effects, resulting in faster stabilization of displacement. This effect enhances the material's response by making it more localized over time and space, which is beneficial for applications that require quick recovery or dynamic stability.

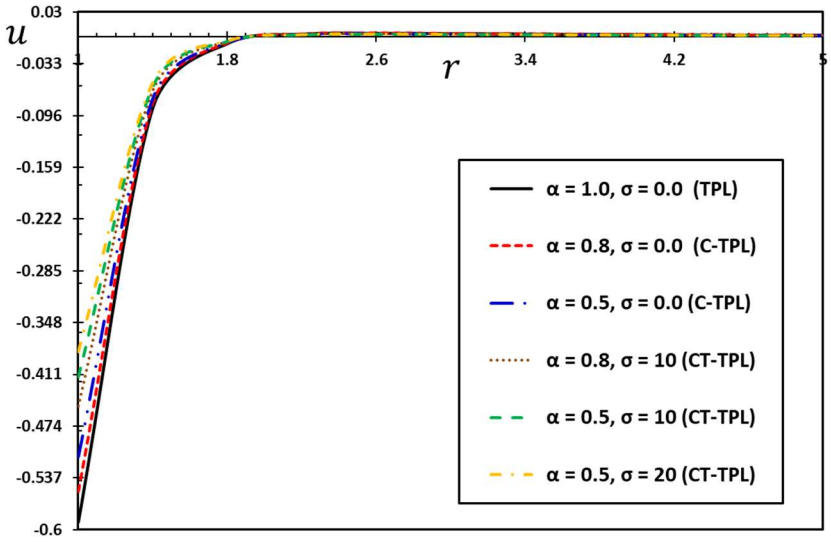

Figure 3. Displacement (u) variations with fractional order (α) and tempering (σ) parameters.

The interplay between the fractional order (α) and tempering parameter (σ) allows for precise tuning of the material's mechanical response. For example, a combination of low α and high σ creates a highly damped response with rapid stabilization, ideal for applications like vibration damping or shock absorption. Conversely, high α combined with low σ results in a more traditional elastic reaction with slower stabilization, beneficial for scenarios needing prolonged deformation.

Initially, at smaller radial distances ($r = 1$), the displacement values are negative, indicating inward movement due to thermal and mechanical loading near the cavity. The radial displacement (u) shows a clear correlation with radial distance (r). At smaller radial distances ($r = 1$), displacement values manifest the greatest magnitude due to proximity to the spherical cavity, where thermal and mechanical interactions are most intense. As r increases, the displacement consistently decreases, suggesting that the influence of the cavity lessens with distance. The decay rate is determined by both the fractional order (α) and tempering parameter (σ), with lower α values and higher σ values resulting in steeper declines in displacement, highlighting stronger memory effects and quicker stabilization.

Manipulating the fractional order (α) and the tempering parameter (σ) provides a powerful approach to customizing the mechanical characteristics of porous materials. By fine-tuning these parameters, engineers can develop materials specifically suited for various applications. For instance,

in dynamic systems, higher σ values allow for quick stabilization, which is essential for effective vibration damping or dynamic thermal management. Meanwhile, lower α values can improve energy absorption capabilities, making the materials particularly effective for resisting impacts. Additionally, materials designed with lower α can demonstrate reduced heat dissipation, making them well-suited for applications requiring thermal insulation or heat retention.

Figure 4 presents the radial nonlocal thermal stresses (T_{rr}) and examines how these stresses depend on the type of fractional derivative, alongside the fractional order (α) and the exponential tempering parameter (σ). This analysis reveals critical insights into the behavior of thermal stresses in porous materials under varying conditions. Examining the stress distribution specifically near the cavity surface (at $r = 1$), it is notable that T_{rr} remains zero across all scenarios. This observation aligns with the established boundary condition for a traction-free cavity surface, where no thermal stress is exerted. As one moves just outside of the cavity ($r > 1$), thermal stress begins to emerge, peaking at $r = 1.4$ before gradually tapering off with increasing radial distance. This pattern emphasizes the critical role of proximity to the cavity in determining the distribution of thermal stresses within the material. The radial thermal stress (T_{rr}) shows a distinct correlation with radial distance (r). At smaller distances, particularly at $r = 1.4$, the stress values are at their highest, indicating the significant impact of thermal and mechanical disturbances close to the spherical cavity. As the distance from the cavity increases, stress levels decrease steadily, illustrating that the influence of the cavity weakens with greater separation.

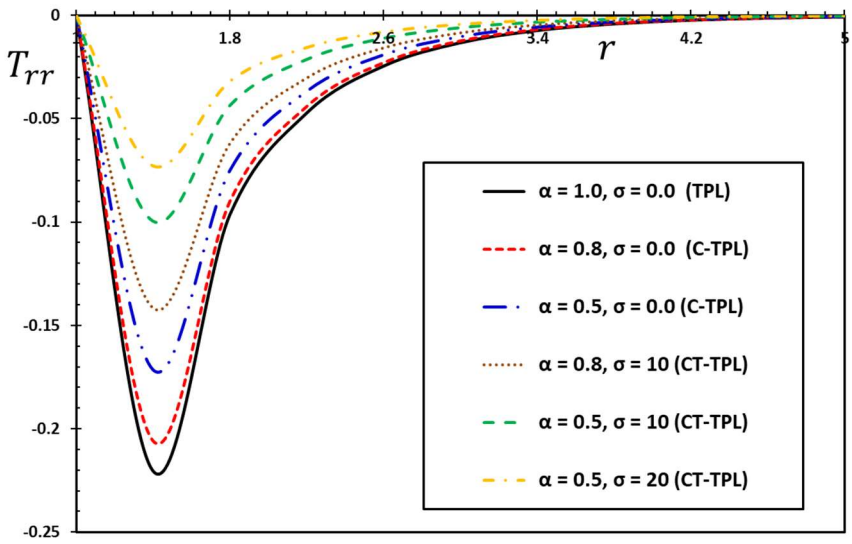

Figure 4. Nonlocal stress (T_{rr}) variations with fractional order (α) and tempering (σ) parameters.

When the tempering parameter (σ) is held constant at 0.0, lowering the fractional order (α) from 1.0 to 0.5 results in a reduction of the radial thermal stress (T_{rr}) across all radial distances (r). For instance, at $r = 1.4$, T_{rr} decreases from -0.220284 (when $\alpha = 1.0$) to -0.171524 (when $\alpha = 0.5$). This trend indicates that lower fractional orders ($\alpha < 1$) tend to enhance memory effects, which contribute to slower stress relaxation and a longer retention of thermal stresses. As α approaches 1, the decay of stress occurs more swiftly, reflecting behavior characteristics of classical mechanics, where memory effects become less significant.

With a fixed fractional order (α), an increase in the tempering parameter (σ) leads to a notable

decrease in the magnitude of radial thermal stress (T_{rr}). For example, at r = 1.4 and α = 0.5, T_{rr} drops from -0.171524 (for σ = 0.0) to -0.072994 (for σ = 20). The exponential tempering factor $e^{-\sigma x}$ plays a critical role in accelerating the decay of memory effects, resulting in faster stress relaxation and a more localized response in the material. This characteristic makes the material particularly advantageous for applications that necessitate quick thermal recovery or minimized residual stresses.

The interaction between α and σ enables precise adjustment of the material's thermoelastic behavior. For instance, utilizing a combination of low α and high σ leads to a significantly damped response characterized by swift stress relaxation. This configuration is particularly beneficial for applications like thermal shock resistance or vibration damping, where quick recovery from mechanical or thermal loads is essential. On the other hand, employing a combination of high α and low σ yields a more traditional elastic response, marked by slower stress relaxation. This setup is ideal for scenarios that demand sustained stress retention, making it suitable for applications where stability and long-term performance are critical.

Figure 5 illustrates the variation of the volume fraction field (ϕ) in relation to the radius within a porous infinite elastic material featuring a spherical cavity. This representation highlights the dependence of the volume fraction on several factors, including the type of fractional derivative, the fractional order (α), and the exponential smoothing factor (σ). The volume fraction field (ϕ) clearly varies with radial distance (r). At smaller distances, specifically at r = 1, the volume fraction ϕ reaches its peak values, highlighting the significant impact of thermal and mechanical disturbances near the spherical cavity. As one moves further away and r increases, there is a steady decline in the volume fraction ϕ, signifying that the effect of the cavity weakens with increasing distance.

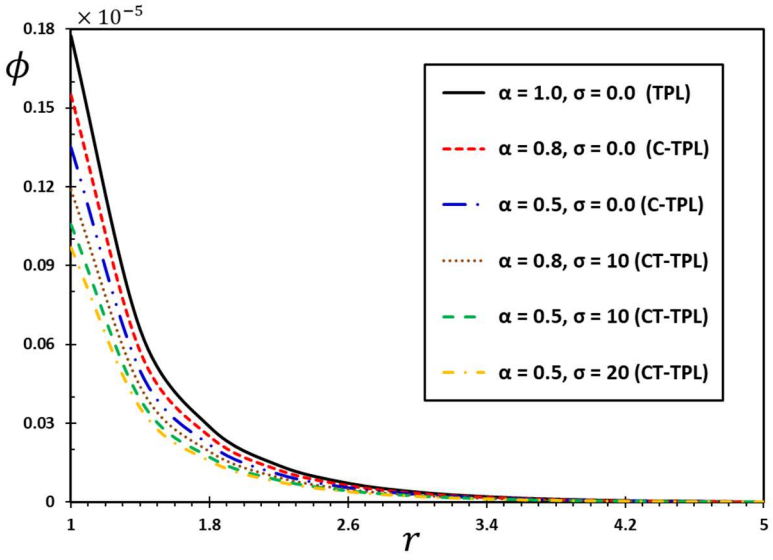

Figure 5. Volume fraction (ϕ) variations with fractional order (α) and tempering (σ) parameters.

When the tempering parameter (σ) is held constant at 0.0, decreasing the fractional order (α) from 1.0 to 0.5 results in a reduction of the volume fraction field (ϕ) at all radial distances (r). For instance, at r = 1, ϕ drops from 0.177517 (with α = 1.0) to 0.13496 (with α = 0.5). This trend indicates that lower fractional orders (α < 1) strengthen memory effects, which leads to a slower evolution of the volume fraction field ϕ and a longer retention of previous conditions. As α nears 1, the volume fraction field stabilizes more rapidly, showcasing behavior akin to classical mechanics, where memory

effects play a diminished role.

With a fixed fractional order (α), an increase in the tempering parameter (σ) markedly decreases the volume fraction field (ϕ). For example, at r = 1 and α = 0.5, ϕ reduces from 0.13496 (for σ = 0.0) to 0.096955 (for σ = 20). The exponential tempering factor $e^{-\sigma}$ accelerates the fading of memory effects, resulting in a quicker stabilization of the volume fraction field. This characteristic lends the material a more localized temporal and spatial response, making it particularly suited for applications that require swift recovery or dynamic stability.

8.2. Influence of internal length scale and time scale parameters

The internal length scale (η) serves as a vital metric that indicates how the surrounding material points influence a specific location within a substance. This parameter is particularly significant in the context of wave dispersion and size-dependent phenomena, which are commonly observed in nanostructures. Here, the microstructural characteristics greatly shape the material's overall response to external stimuli. The characteristic time scale (ζ), on the other hand, captures the essence of time-delayed interactions, accounting for the lag between the application of loads and the resulting responses of the material. This aspect becomes crucial when modeling dynamic situations, such as the heat fluxes generated by laser pulses, where transient effects play a dominant role.

In the classical framework where both η and ζ are set to zero, the system defaults to the local two-phase lag (FTPL) thermoelastic model that incorporates fractional derivatives. In this scenario, the responses are strictly determined by the local thermal and mechanical properties, effectively ignoring the influences of spatial nonlocality and time scale effects. Stress and strain fields rely solely on nearby temperature gradients and deformations. However, this approach has its limitations, as it fails to account for wave dispersion and size-dependent effects, overlooking the critical transient delays in heat conduction and stress propagation, especially pertinent in nanoporous materials and scenarios involving laser-induced heat fluxes. In contrast, the nonlocal framework, characterized by non-zero values for both η and ζ, introduces a more nuanced perspective. It leverages the KG operator to incorporate both spatial and temporal nonlocality, enabling responses to be shaped by not just neighboring points but also by historical states of the material. This approach effectively captures size-dependent phenomena, such as stress concentrations near voids and wave scattering, while also modeling time-delayed thermal and mechanical effects. As a result, this framework provides improved accuracy in dynamic scenarios, making it a more robust choice for understanding complex material behaviors.

Figure 6 illustrates the impact of the intrinsic length scale (η) and characteristic time scale (ζ) on the non-dimensional temperature distribution (θ) as a function of radial distance (r). The figure demonstrates the interaction between spatial nonlocality (η) and temporal nonlocality (ζ), showing how these parameters influence the temperature distribution within a porous medium.

In the standard scenario, where both η and ζ are set to zero, the system behaves in line with classical local models that exclude any spatial or temporal nonlocal effects. Here, the highest temperature values emerge because heat diffusion operates without the complexities introduced by size or time-dependent memory effects. Conversely, in nonlocal scenarios where η is greater than zero and ζ is non-negative, there is a noticeable decline in temperature readings. Increasing the internal length scale (η), which introduces spatial nonlocality, along with the characteristic time scale (ζ), which accounts for temporal nonlocality, leads to diminished temperature values. This reduction arises from the interplay of spatial averaging and the delayed propagation of heat, resulting in slower heat diffusion and lower peak temperatures.

Radially, the temperature consistently decreases as the radial distance increases. Close to the

cavity, at a radial distance of r = 1, the temperature is significantly higher due to concentrated thermal interactions. However, as one moves outward to larger distances, such as r = 5, the temperature experiences substantial decay, reflecting smaller values. Specifically examining the impact of η and ζ, in the absence of nonlocal effects (η = 0.000, ζ = 0.000), the temperature follows a predictable decreasing trend with respect to radial distance, illustrating classical heat conduction behavior. As η increases, the temperature consistently decreases across all radial distances, especially pronounced near the cavity. For instance, at r = 1, the temperature drops from 0.796883 (η = 0.000) to 0.739311 when η is increased to 0.004 and ζ to 0.003. In a similar vein, higher ζ values further reduce temperature, notably beyond r = 1.4, as evidenced by a decrease from 0.0163379 (η = 0.000, ζ = 0.000) to 0.0128245 (η = 0.004, ζ = 0.005) at r = 3.

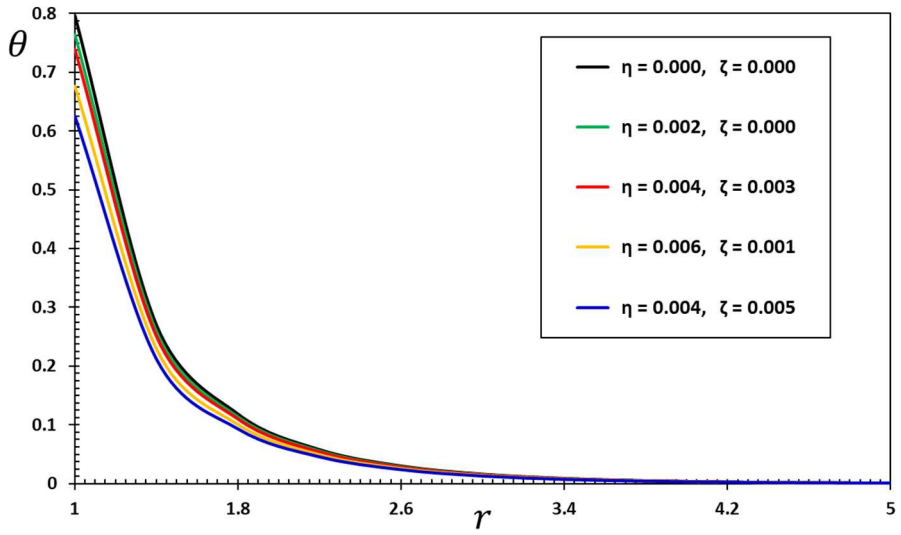

Figure 6. Temperature (θ) variations with space-time nonlocality parameters (η and ζ).

The intrinsic length scale (η) plays a pivotal role in introducing spatial nonlocality, affecting each location's temperature by factoring in the influence of surrounding material points. This leads to increased spatial averaging, effectively smoothing temperature gradients and lowering peak values. Most prominently, this effect is observed near the cavity, where localized thermal conditions are spread over a broader area. As η escalates from 0.002 to 0.006, the temperature decreases across all radial distances, with the most significant reductions appearing close to the cavity.

In terms of the characteristic time scale (ζ), this parameter brings temporal nonlocality into the model, taking into account the delay in heat propagation over time. Higher ζ values result in slower thermal diffusion, which manifests as lower temperature readings because it takes longer for heat to reach an equilibrium state. This impact is particularly observable at greater radial distances, such as those beyond r = 2, where the delays play a significant role. As ζ progresses from 0.000 to 0.005, a decrease in temperature becomes evident, particularly in areas farther from the cavity.

The combined influence of η and ζ accentuates the nonlocal characteristics of the model. Elevated η values work to decrease the temperature by spatially averaging the thermal profile, while increased ζ values contribute to this decline by introducing delays in heat diffusion. For instance, at r = 1, the temperature descends from 0.796883 (η = 0.000, ζ = 0.000) to 0.625518 (η = 0.004, ζ = 0.005), illustrating the compounded effects of spatial and temporal nonlocality.

The findings hold several practical implications. For thermal insulation, materials characterized

by higher values of η and ζ display slower heat diffusion and reduced peak temperatures, making them particularly suitable for insulation purposes. In dynamic thermal management systems, the delays in heat propagation associated with higher ζ values could be advantageous for applications requiring gradual heat dissipation, such as in electronics or nanostructured components. Lastly, incorporating nonlocal parameters such as η and ζ is crucial in accurately modeling the behavior of nanoporous materials, where size and time-dependent effects are critical considerations in their thermal responses.

Figure 7 examines the impact of the intrinsic length scale (η) and characteristic time scale (ζ) on the dimensionless displacement (u) within an infinite nanoelastic medium that contains a spherical cavity. The curves in Figure 7 illustrate the behavior of u as a function of the radial distance (r) for various combinations of η and ζ. The radial displacement (u) exhibits complex patterns that vary with the radial distance (r), the intrinsic length scale (η), and the characteristic time scale (ζ). At smaller radial distances (around $r = 1$), the displacement is negative, indicating inward movement due to thermal and mechanical influences near the cavity. As r increases, u becomes positive, signifying outward movement caused by the same loading effects. The magnitude of u diminishes with increasing r, showing that the cavity's influence lessens at greater distances.

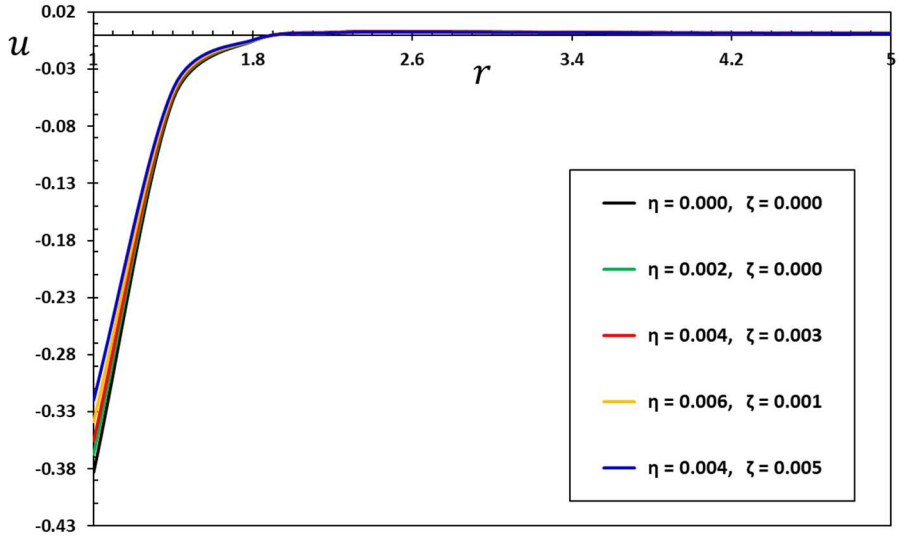

Figure 7. Displacement (u) variations with space-time nonlocality parameters (η and ζ).

In the standard scenario (η = 0, ζ = 0), the system behaves like a classical local model, displaying the largest displacement magnitudes. Near $r = 1$, significant negative values are observed due to the absence of spatial or temporal nonlocal effects, meaning displacement (u) depends only on local mechanical properties. However, when η and ζ are non-zero, the displacement magnitude decreases both near the cavity and at larger distances. This reduction is due to the smoothing effect of spatial nonlocality (η) and the damping effect introduced by temporal nonlocality (ζ).

The intrinsic length scale (η) plays a critical role in shaping displacement (u) behavior. As η increases, it promotes spatial averaging, reducing the localization of mechanical responses and resulting in a smoother displacement field (u), especially near the cavity. For example, at $r = 1$, as η increases from 0.000 to 0.006 (with ζ = 0.001), the inward displacement (u) decreases from −0.383079 to −0.338451. At larger distances ($r > 3$), the influence of η diminishes as displacement values become inherently small. For instance, at $r = 4.6$, the displacement u decreases slightly from 0.00159686 (η = 0.000) to 0.00141083 (η = 0.006, ζ = 0.001).

Similarly, the characteristic time scale (ζ) introduces time-delay effects that further dampen mechanical responses. As ζ increases, the stabilization of the displacement field (u) slows down, particularly at larger radial distances. For example, near $r = 1$, increasing ζ reduces inward displacement (u) from −0.355403 (η = 0.004, ζ = 0.003) to −0.320056 (η = 0.004, ζ = 0.005). At greater distances, such as $r = 5$, the damping effect of ζ becomes more pronounced, with u decreasing from 0.00130603 (η = 0.004, ζ = 0.003) to 0.00117 (η = 0.004, ζ = 0.005).

The interaction between η and ζ amplifies the overall nonlocal effects in the model. Higher η values redistribute mechanical responses spatially, while higher ζ values introduce delays, enhancing displacement dampening. For instance, at $r = 1$, the displacement (u) decreases from −0.383079 (classical case, η = 0.000, ζ = 0.000) to −0.320056 (η = 0.004, ζ = 0.005), illustrating the combined effects of these parameters.

These findings have significant practical implications. Materials with higher η and ζ values exhibit reduced displacement magnitudes and faster stabilization, making them ideal for applications requiring effective vibration damping or shock absorption. Additionally, the influence of η and ζ is crucial for modeling nanostructured materials, where size- and time-dependent effects dominate. The ability to control temporal nonlocality (ζ) also allows for precise management of time-delayed mechanical responses, enabling the design of materials with enhanced dynamic stability for various advanced applications.

Figure 8 illustrates the nonlocal, non-dimensional thermal stress distribution (T_{rr}) for various values of the intrinsic length scale (η) and characteristic time scale (ζ). The figure highlights the influence of spatial and temporal nonlocality on the size- and time-dependent stress behavior of materials with nanoscale characteristics. From the analysis presented in Figure 8, it is clear that at a radial distance of $r = 1$, the thermal radial stress (T_{rr}) remains at zero, regardless of the configurations of η and ζ. This observation aligns perfectly with the condition of a free-traction boundary, where no stress is exerted at that surface. Beyond this point, T_{rr} takes on negative values, which signify compressive stress arising from thermal expansion effects. Moreover, as the radial distance increases, the magnitude of T_{rr} decreases, illustrating the diminishing impact of the cavity with distance.

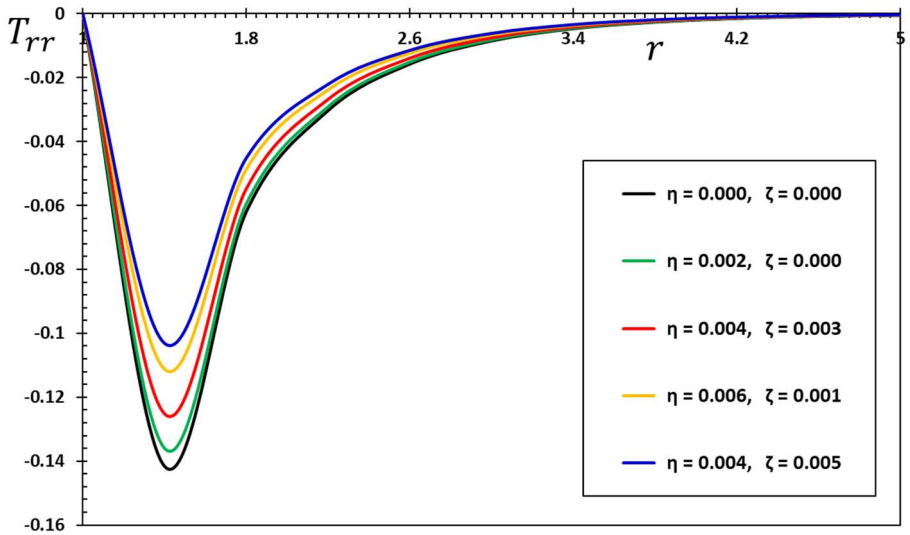

Figure 8. Nonlocal thermal stress (T_{rr}) variations with space-time nonlocality parameters (η and ζ).

In the benchmark scenario where both η and ζ equal zero, the results in Figure 8 display adherence to the classical local model, revealing that the thermal stress T_{rr} achieves its peak value in the absence of nonlocal effects. When delving into nonlocal scenarios where η is positive and ζ is non-negative, Figure 8 indicates a noticeable reduction in the magnitude of T_{rr}, both close to the cavity at r = 1.4 and further out at r = 5. This decrease is caused by the smoothing effects related to spatial nonlocality (η) and the damping effects associated with temporal nonlocality (ζ).

As η increases, the stress gradients illustrated in Figure 8 become more uniform, leading to a reduction in stress concentrations near the cavity's surface. For example, at r = 1.4, the thermal stress T_{rr} diminishes from -0.141646 (when η = 0.000) to -0.111186 (at η = 0.006 and ζ = 0.001). Even at a greater radial distance of r = 5, the stress T_{rr} decreases from -0.000533963 (η = 0.000) to -0.000419138 (η = 0.006, ζ = 0.001), though the effect is less pronounced. The characteristic time scale represented by ζ introduces temporal nonlocality, which accounts for delays in stress propagation. In Figure 8, it is depicted that larger values of ζ lead to lower stress magnitudes, indicating a delay in the system's response to thermal and mechanical loads. For instance, at r = 1.4, the thermal stress T_{rr} falls from -0.125144 (with η = 0.004 and ζ = 0.003) to -0.10307 (with η = 0.004 and ζ = 0.005). This damping effect becomes even more evident at r = 5, where the stress T_{rr} reduces from -0.000471757 (η = 0.004, ζ = 0.003) to -0.000388546 (η = 0.004, ζ = 0.005).

Additionally, Figure 8 highlights the interactive effects of η and ζ on the thermal stress T_{rr}. Higher values of η contribute to the spatial redistribution of thermal effects, while elevated ζ values further diminish stress through delayed mechanical responses. This interaction is particularly significant near the cavity, such as at r = 1.4 but begins to wane at extended distances. For example, the thermal stress T_{rr} decreases from -0.141646 (in the absence of nonlocal effects) to -0.10307 (when incorporating both η = 0.004 and ζ = 0.005), illustrating how spatial and temporal nonlocality cooperatively smooth and weaken the stress distributions.

These insights carry substantial practical implications. Materials with increased values of η and ζ tend to show diminished stress concentrations and smoother stress distributions, significantly enhancing resistance to thermal shocks. In the realm of nanostructured materials, recognizing the contributions of spatial and temporal nonlocality is essential for accurately modeling stress behavior, especially in contexts where size and time-dependent phenomena are critical. Moreover, the influence of temporal nonlocality (ζ) facilitates controlled stress relaxation, thus boosting the dynamic stability of materials subjected to sudden loading conditions (an important attribute for numerous engineering applications).

Figure 9 illustrates the impact of the intrinsic length scale (η) and characteristic time scale (ζ) on the distribution of the non-dimensional volume fraction field (ϕ) within an infinite elastic medium containing a spherical cavity. This analysis investigates how spatial nonlocality (η) and temporal nonlocality (ζ) affect the evolution of ϕ, which represents the void or porosity field. The volume fraction field (ϕ) is a critical parameter in porous materials, as it indicates the distribution of voids under thermoelastic loading conditions.

Close to the cavity (at r = 1), the volume fraction field (ϕ) reaches its highest value due to the significant thermal and mechanical interactions occurring near the spherical cavity. However, as the parameters η and ζ increase, ϕ begins to decline, demonstrating the dampening effects of both spatial and temporal nonlocality. Moving farther from the cavity (when r > 1), ϕ consistently decreases as the radial distance increases, indicating that the impact of the cavity lessens with distance. The rate at which ϕ decays is influenced by both η and ζ, as larger values of these parameters promote smoother and more subdued distributions.

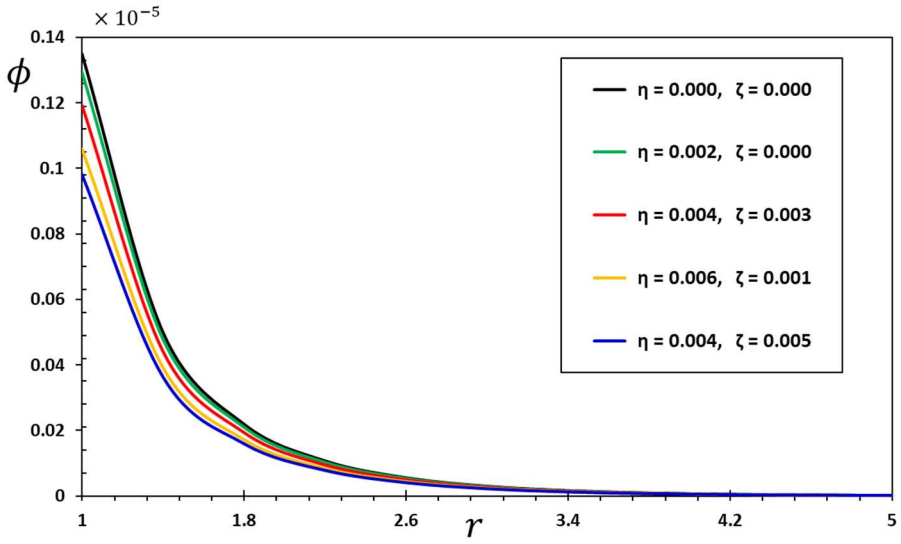

Figure 9. Volume fraction field (ϕ) variations with space-time nonlocality parameters (η and ζ).

In the standard scenario (η = 0.000, ζ = 0.000), the results illustrate a classical local model where ϕ is maximized across all radial distances since no nonlocal effects are considered. Here, the behavior is predominantly determined by local thermal and mechanical properties, showcasing sharp gradients near the cavity. When η and ζ are greater than zero, the introduction of spatial (η) and temporal (ζ) nonlocality leads to a noticeable reduction in ϕ values throughout all radial distances, especially in close proximity to the cavity. Increasing η and ζ smooths the spatial layout of ϕ, reducing peak values near $r = 1$ and signifying a more gradual evolution of voids due to the influences of nonlocal interactions.

Understanding the physical interpretation of η shows that it introduces spatial nonlocality, where the state at a particular point is affected not only by local conditions but also by the neighboring areas. An increase in η results in smoother distributions, as the void fraction field becomes more averaged out. Near $r = 1$, it is noted that an increase in η leads to a decrease in ϕ. Specifically, ϕ diminishes from 0.13496 when η = 0.000 to 0.105938 with η = 0.006 and ζ = 0.001. As the distance from the cavity increases ($r > 3$), the influence of η diminishes; for example, at $r = 3$, ϕ decreases from 0.00302298 with η = 0.000 to 0.00237291 with η = 0.006 and ζ = 0.001.

The influence of ζ introduces temporal nonlocality, accounting for the delays that occur in the evolution of voids. Higher values of ζ effectively dampen the evolution of ϕ, leading to a slower response to thermal and mechanical stimuli. As observed near the cavity (at $r = 1$), increasing ζ decreases ϕ even further; for instance, it shifts from 0.119238 (η = 0.004, ζ = 0.003) to 0.0982058 (η = 0.004, ζ = 0.005). At greater distances (specifically $r = 5$), the damping effect of ζ is particularly significant, with ϕ declining from 0.000166467 (η = 0.004, ζ = 0.003) to 0.000137104 (η = 0.004, ζ = 0.005).

The interplay between η and ζ yields a powerful impact. Spatial nonlocality (η) reduces the highest values of ϕ and smooths out its distribution, while temporal nonlocality (ζ) adds further damping by inducing time delays. This combination is most pronounced near the cavity, where the evolution of the void fraction field occurs more gradually due to the synergistic effects of spatial and temporal influences. For example, at $r = 1$, ϕ decreases from 0.13496 (with η = 0.000 and ζ = 0.000) to 0.0982058 (with η = 0.004 and ζ = 0.005).

The insights gained from these findings offer substantial practical implications. With larger values of η and ζ, the resulting void fraction distributions become smoother and more damped. This

characteristic is crucial for controlling localized void growth and enhancing the structural integrity of porous materials. Additionally, the dampening implications attributed to η and ζ help minimize peak values of ϕ, reducing stress concentrations and bolstering the overall stability of materials under thermal and mechanical loading. In the design of nanostructures, recognizing the role of spatial and temporal nonlocality is essential for accurately modeling void evolution, especially in scenarios where size and time-dependent effects play a dominant role.

9. Conclusions

This study examined the Caputo-tempered two-phase lag (FCT-TPL) heat conduction model and its influence on thermoelastic vibrations in materials containing spherical cavities and voids. By integrating fractional calculus and tempered derivatives, along with spatial and temporal nonlocality, the model effectively bridges the gap between classical and generalized thermoelastic theories, offering a robust framework for accurately analyzing size-dependent phenomena and wave scattering.

The results demonstrate that the distinction between the fractional Caputo (C) and tempered Caputo (CT) derivatives highlights the versatility of fractional calculus in modeling thermoelastic behaviors. Additionally, it is revealed that the fractional-order parameter and the stiffness parameter in differential actuators serve as effective tools for adjusting memory effects, thermal relaxation, and mechanical stability in porous materials. Notably, it is observed that employing low-fractional-order values in combination with high-stiffness parameter values leads to rapid attenuation of responses, making this configuration particularly advantageous for applications requiring dynamic stability and efficient vibration damping. Conversely, utilizing high-fractional-order values alongside low stiffness parameter values results in prolonged response durations, which is ideal for applications involving thermal insulation and long-term material performance. This capability to fine-tune material behaviors through these parameters underscores the immense potential of fractional calculus in real-world engineering and material design applications.

From the study and analysis, it is evident that the integration of the parameters η and ζ is crucial for accurately modeling size- and time-dependent phenomena in porous nanomaterials, where localized effects are highly significant. Higher values of spatial nonlocality are shown to enhance spatial averaging, resulting in smoother gradients (e.g., temperature, displacement, and stress) while simultaneously reducing peak magnitudes around localized features such as cavities. Moreover, increasing values of temporal nonlocality introduces time-dependent damping, which slows heat diffusion, stabilizes displacement, and influences void evolution.

The findings conclude that the interaction between spatial nonlocality and temporal nonlocality substantially improves the precision of material modeling under thermoelastic loading. These parameters effectively capture size-dependent behaviors and time-delayed responses, establishing them as indispensable tools in the design of materials with enhanced thermal, mechanical, and structural properties.

While the Caputo-tempered two-phase lag (FCT-TPL) heat conduction model effectively addresses size- and time-dependent phenomena, it faces notable challenges. These include high computational complexity from fractional calculus and nonlocal parameters, sensitivity to parameter calibration, and limited applicability to heterogeneous or anisotropic materials due to its assumptions of homogeneity and isotropy. Additionally, insufficient experimental validation across diverse materials and conditions limits its practical use.

Future advancements should focus on reducing computational demands through efficient numerical methods or machine learning, extending the model to handle irregular geometries and

anisotropy, and integrating it with additional physical phenomena. Comprehensive experimental validation, refined parameter identification techniques, and exploration of applications in emerging technologies are essential. Incorporating nonlinear effects could further enhance its accuracy and relevance, particularly under extreme conditions, solidifying its value in engineering applications.

Author contributions

Kareem Alanazi and Ahmed E. Abouelregal contributed to the conceptualization, methodology, and investigation of the study; Kareem Alanazi focused on data analysis, visualization, and preparing the initial manuscript draft; Ahmed E. Abouelregal provided oversight, critical revisions, and theoretical insights to enhance the interpretation of results. Both authors reviewed and approved the final manuscript. All authors have read and approved the final version of the manuscript for publication.

Use of Generative-AI tools declaration

The authors declare they have not used Artificial Intelligence (AI) tools in the creation of this article.

Conflict of interest

The authors declare no conflict of interest.

References

1. W. Pabst, The linear theory of thermoelasticity from the viewpoint of rational thermomechanics, *Cera.-Silikaty*, **49** (2005), 242–251. Available from: https://www.ceramics-silikaty.cz/index.php?page=cs_detail_doi&id=611.
2. W. Nowacki, *Dynamic problems of thermoelasticity*, Springer Science & Business Media, 1975.
3. Q. Wang, S. Ge, D. Wu, H. Ma, J. Kang, M. Liu, et al., Evolution of microstructural characteristics during creep behavior of Inconel 718 alloy, *Mater. Sci. Eng. A*, **857** (2022), 143859. https://doi.org/10.1016/j.msea.2022.143859
4. D. Y. Tzou, A unified field approach for heat conduction from macro-to micro-scales, *ASME J. Heat Transfer*, **117** (1995), 8–16. https://doi.org/10.1115/1.2822329
5. D. Y. Tzou, *Macro-to microscale heat transfer: the lagging behavior*, John Wiley & Sons, 2014.
6. D. Y. Tzou, The generalized lagging response in small-scale and high-rate heating, *Int. J. Heat Mass Transfer*, **38** (1995), 3231–3240. https://doi.org/10.1016/0017-9310(95)00052-B
7. H. W. Lord, Y. Shulman, A generalized dynamical theory of thermoelasticity, *J. Mech. Phys. Solids*, **15** (1967), 299–309. https://doi.org/10.1016/0022-5096(67)90024-5
8. A. E. Green, K. Lindsay, Thermoelasticity, *J. Elasticity*, **2** (1972), 1–7. https://doi.org/10.1007/BF00045689
9. M. Shariati, M. Shishesaz, H. Sahbafar, M. Pourabdy, M. Hosseini, A review on stress-driven nonlocal elasticity theory, *J. Comput. Appl. Mech.*, **52** (2021), 535–552. https://doi.org/10.22059/jcamech.2021.331410.653
10. A. C. Eringen, J. L. Wegner, Nonlocal continuum field theories, *Appl. Mech. Rev.*, **56** (2003), B20–B22. https://doi.org/10.1115/1.1553434

11. C. Polizzotto, Stress gradient versus strain gradient constitutive models within elasticity, *Int. J. Solids Struct*., **51** (2014), 1809–1818. https://doi.org/10.1016/j.ijsolstr.2014.01.021
12. E. C. Aifantis, Gradient deformation models at nano, micro, and macro scales, *J. Mech. Behav. Mater*., **121** (1999), 189–202. https://doi.org/10.1115/1.2812366
13. F. A. C. M. Yang, A. C. M. Chong, D. C. C. Lam, P. Tong, Couple stress based strain gradient theory for elasticity, *Int. J. Solids Struct*., **39** (2002), 2731–2743. https://doi.org/10.1016/S0020-7683(02)00152-X
14. C. W. Lim, G. Zhang, J. Reddy, A higher-order nonlocal elasticity and strain gradient theory and its applications in wave propagation, *J. Mech. Phys. Solids*, **78** (2015), 298–313. https://doi.org/10.1016/j.jmps.2015.02.001
15. S. Li, W. Zheng, L. Li, Spatiotemporally nonlocal homogenization method for viscoelastic porous metamaterial structures, *Int. J. Mech. Sci*., **282** (2024), 109572.
16. A. Overvig, S. A. Mann, A. Alù, Spatio-temporal coupled mode theory for nonlocal metasurfaces, *Light: Sci. Appl*., **13** (2024), 28. https://doi.org/10.1038/s41377-023-01350-9
17. Y. Zhang, D. Nie, X. Mao, L. I. Li, A thermodynamics-consistent spatiotemporally-nonlocal model for microstructure-dependent heat conduction, *Appl. Math. Mech*., **45** (2024), 1929–1948. https://doi.org/10.1007/s10483-024-3180-7
18. A. E. Abouelregal, M. Marin, A. Öchsner, A modified spatiotemporal nonlocal thermoelasticity theory with higher-order phase delays for a viscoelastic micropolar medium exposed to short-pulse laser excitation, *Continuum Mech. Thermodyn*., **37** (2025), 15. https://doi.org/10.1007/s00161-024-01342-z
19. A. E. Abouelregal, M. Marin, Y. Alhassan, D. Atta, A novel space–time nonlocal thermo-viscoelastic model with two-phase lags for analyzing heat diffusion in a half-space subjected to a heat source, *Iran. J. Sci. Technol. Trans. Mech. Eng*., **49** (2025), 1315–1332. https://doi.org/10.1007/s40997-025-00835-9
20. M. Lazar, E. Agiasofitou, Nonlocal elasticity of Klein–Gordon type: Fundamentals and wave propagation, *Wave Motion*, **114** (2022), 103038. https://doi.org/10.1016/j.wavemoti.2022.103038
21. E. Agiasofitou, M. Lazar, Nonlocal elasticity of Klein–Gordon type with internal length and time scales: Constitutive modelling and dispersion relations, *PAMM*, **23** (2023), e202300065. https://doi.org/10.1002/pamm.202300065
22. A. A. Kilbas, H. M. Srivastava, J. J. Trujillo, *Theory and applications of fractional differential equations*, Elsevier, 2006.
23. M. Caputo, M. Fabrizio, A new definition of fractional derivative without singular kernel, *Prog. Fract. Differ. Appl*., **1** (2015), 73–85. http://dx.doi.org/10.12785/pfda/010201
24. M. Caputo, M. Fabrizio, Applications of new time and spatial fractional derivatives with exponential kernels, *Prog. Fract. Differ. Appl*., **2** (2016), 1–11. http://dx.doi.org/10.18576/pfda/020101
25. A. Atangana, D. Baleanu, Caputo-Fabrizio derivative applied to groundwater flow within confined aquifer, *J. Eng. Mech*., **143** (2017), D4016005. https://doi.org/10.1061/(ASCE)EM.1943-7889.0001091
26. A. Atangana, D. Baleanu, New fractional derivatives with nonlocal and non-singular kernel: Theory and application to heat transfer model, *Therm. Sci*., **20** (2016), 763–769. https://doi.org/10.2298/TSCI160111018A
27. S. Saifullah, A. Ali, A. Khan, K. Shah, T. Abdeljawad, A novel tempered fractional transform: Theory, properties and applications to differential equations, *Fractals*, **31** (2023), 2340045. https://doi.org/10.1142/S0218348X23400455

28. A. Liemert, A. Kienle, Fundamental solution of the tempered fractional diffusion equation, *J. Math. Phys*., **56** (2015), 113504. https://doi.org/10.1063/1.4935475
29. M. Medve, M. Pospíšil, Generalized Laplace transform and tempered Ψ-Caputo fractional derivative, *Math. Model. Anal*., **28** (2023), 146–162. https://doi.org/10.3846/mma.2023.16370
30. J. Deng, L. Zhao, Y. Wu, Fast predictor-corrector approach for the tempered fractional differential equations, *Numer. Algorithms*, **74** (2017), 717–754. https://doi.org/10.1007/s11075-016-0169-9
31. A. Zavaliangos, L. Anand, Thermo-elasto-viscoplasticity of isotropic porous metals, *J. Mech. Phys. Solids*, **41** (1993), 1087–1118. https://doi.org/10.1016/0022-5096(93)90056-L
32. M. I. Othman, A. Sur, Transient response in an elasto-thermo-diffusive medium in the context of memory-dependent heat transfer, *Waves Rand. Compl. Media*, **31** (2021), 2238–2261. https://doi.org/10.1080/17455030.2020.1737758
33. A. Hobiny, F. S. Alzahrani, I. Abbas, Three-phase lag model of thermo-elastic interaction in a 2D porous material due to pulse heat flux, *Int. J. Numer. Methods Heat Fluid Flow*, **30** (2020), 5191–5207. https://doi.org/10.1108/HFF-03-2020-0122
34. P. Liu, T. He, Dynamic response of thermoelastic materials with voids subjected to ramp-type heating under three-phase-lag thermoelasticity, *Mech. Adv. Mater. Struct*., **29** (2022), 1386–1394. https://doi.org/10.1080/15376494.2020.1821137
35. V. Gupta, M. S. Barak, S. Das, Impact of memory-dependent heat transfer on Rayleigh waves propagation in nonlocal piezo-thermo-elastic medium with voids, *Int. J. Numer. Methods Heat Fluid Flow*, **34** (2024), 1902–1926. https://doi.org/10.1108/HFF-10-2023-0615
36. S. Mondal, A. Sur, Thermo-hydro-mechanical interaction in a poroelastic half-space with nonlocal memory effects, *Int. J. Appl. Comput. Math*., **10** (2024), 68. https://doi.org/10.1007/s40819-024-01717-5
37. F. Ebrahimi, K. Khosravi, A. Dabbagh, A novel spatial–temporal nonlocal strain gradient theorem for wave dispersion characteristics of FGM nanoplates, *Waves Rand. Com. Media*, **34** (2024), 3490–3509. https://doi.org/10.1080/17455030.2021.1979272
38. M. Jia, S. Y. Lou, Integrable nonlinear Klein–Gordon systems with PT nonlocality and/or space–time exchange nonlocality, *Appl. Math. Lett*., **130** (2022), 108018. https://doi.org/10.1016/j.aml.2022.108018
39. B. Singh, Wave propagation in context of Moore–Gibson–Thompson thermoelasticity with Klein–Gordon nonlocality, *Vietnam J. Mech*., **46** (2024), 104–118. https://doi.org/10.15625/0866-7136/19728
40. F. Ebrahimi, K. Khosravi, A. Dabbagh, Wave dispersion in viscoelastic FG nanobeams via a novel spatial–temporal nonlocal strain gradient framework, *Waves Rand. Com. Media*, **34** (2024), 2962–2984. https://doi.org/10.1080/17455030.2021.1970282
41. M. E. Elzayady, A. E. Abouelregal, F. Alsharif, H. Althagafi, M. Alsubhi, Y. Alhassan, Two-stage heat-transfer modeling of cylinder-cavity porous magnetoelastic bodies, *Mech. Time-Depend. Mater.,* **28** (2024), 2819–2840. https://doi.org/10.1007/s11043-024-09691-7
42. L. Anitha, R. M. Devi, R. Selvamani, F. Ebrahimi, Nonlocal couple stress vibration of pasted thermo elastic multilayered cylinder with hall current and multi dual phase lags, *Mech. Solids*, **59** (2024), 1659–1671. https://doi.org/10.1134/S0025654424603045
43. H. Guo, Z. Xu, F. Shang, T. He, A new constitutive theory of nonlocal piezoelectric thermoelasticity based on nonlocal single-phase lag heat conduction and structural transient thermo-electromechanical response of piezoelectric nanorod, *Mech. Adv. Mater. Struct.*, **31** (2024), 11737–11754. https://doi.org/10.1080/15376494.2024.2311240

44. M. Arai, K. Masui, One-dimensional thermo-elastic wave analysis for dynamic thermoelasticity coupled with dual-phase-lag heat conduction model, *Mech. Eng. J.*, **11** (2024), 24-00255. https://doi.org/10.1299/mej.24-00255
45. K. Zakaria, M. A. Sirwah, A. E. Abouelregal, A. F. Rashid, Photothermoelastic interactions in silicon microbeams resting on linear Pasternak foundation based on DPL model, *Int. J. Appl. Mech*., **13** (2021), 2150079. https://doi.org/10.1142/S1758825121500794
46. E. C. D. Oliveira, J. A. Machado, A review of definitions for fractional derivatives and integral, *Math. Probl. Eng*., **2014** (2014), 1–7. https://doi.org/10.1155/2014/238459
47. F. I. A. Amir, A. Moussaoui, R. Shafqat, M. H. El Omari, S. Melliani, The Hadamard ψ-Caputo tempered fractional derivative in various types of fuzzy fractional differential equations, *Soft Comput*., **28** (2024), 9253–9270. https://doi.org/10.1007/s00500-024-09821-w
48. A. E. Abouelregal, Y. Alhassan, S. S. Alsaeed, M. Marin, M. E. Elzayady, MGT photothermal model incorporating a generalized Caputo fractional derivative with a tempering parameter: Application to an unbounded semiconductor medium, *Contemp. Math*., **5** (2024), 6556–6581. https://doi.org/10.37256/cm.5420245963
49. A. E. Abouelregal, M. Marin, A. Foul, S. S. Askar, Thermomagnetic responses of a thermoelastic medium containing a spherical hole exposed to a timed laser pulse heat source, *Case Stud. Therm. Eng*., **56** (2024), 104288. https://doi.org/10.1016/j.csite.2024.104288
50. A. Kuznetsov, On the convergence of the Gaver–Stehfest algorithm, *SIAM J. Numer. Anal*., **51** (2013), 2984–2998. https://doi.org/10.1137/13091974X
51. F. A. S. Martins, G. J. Weymar, I. da Cunha Furtado, F. Tumelero, R. da Silva Brum, R. S. de Quadros, et al., Analysis of EAHE through a coupled mathematical model solved by Laplace transform and Gaver-Stehfest algorithm, *Cienc. Nat*., **45** (2023), e74745. https://doi.org/10.5902/2179460X74745
52. S. Sheikh, L. Khalsa, G. Makkad, V. Varghese, Fractional dual-phase-lag hygrothermoelastic model for a sphere subjected to heat-moisture load, *Arch. Appl. Mech*., **94** (2024), 1379–1396. https://doi.org/10.1007/s00419-024-02583-9
53. Z. Xue, H. Zhang, J. Liu, M. Wen, Thermoelastic response of porous media considering spatial scale effects of heat transfer and deformation, *J. Eng. Mech*., **151** (2025), 05024002. https://doi.org/10.1061/JENMDT.EMENG-7730
54. R. A. Fathy, E. E. Eraki, M. I. Othman, Effects of rotation and nonlocality on the thermoelastic behavior of micropolar materials in the 3PHL model, *Iran. J. Sci. Technol. Trans. Mech. Eng*., **49** (2025), 165–180. https://doi.org/10.1007/s40997-025-00834-w